Significant equatorial plasma bubbles and global ionospheric disturbances after the 2022 Tonga volcano eruption

Ercha Aa[1], Shun-Rong Zhang[1], Philip J. Erickson[1], Juha Vierinen[2], Anthea J. Coster[1], Larisa P. Goncharenko[1], Andres Spicher[2], and William Rideout[1]

[1]Haystack Observatory, Massachusetts Institute of Technology, Westford, MA, USA.
[2]Department of Physics and Technology, The Arctic University of Norway, Tromsø, Norway

Key Points:

- Large 5–10 TECU depletion was observed near Tonga epicenter by accurate Beidou GEO data, consisting of cascading TEC drops and oscillations
- TEC rate of change index revealed globally propagating ionospheric disturbances, with shock fronts traveling at Lamb wave speeds of 315 m/s
- Pronounced and prolonged post-volcanic equatorial plasma bubbles were observed over Asia-Oceania area, covering 100°+ longitudinal range

Corresponding author: E. Aa, `aercha@mit.edu`

Abstract

This paper investigates local and global ionospheric responses to the 2022 Tonga volcano eruption, using ground-based Global Navigation Satellite System (GNSS) total electron content (TEC) and Swarm in-situ measurements. The main results are as follows: (1) A significant local ionospheric depletion of 5–10 TECU was observed near the epicenter, comprising of several cascading TEC decreases and quasi-periodic oscillations. (2) The eruption triggered various acoustic-gravity waves manifesting as travelling ionospheric disturbances (TIDs) with velocities of 180–1050 m/s; the prevailing Lamb-wave mode propagated globally at ∼315 m/s and caused significant global-scale ionospheric disturbances. (3) Pronounced post-volcanic nighttime equatorial plasma bubbles (EPBs) were observed in the Asian-Oceania area after arrival of volcano-induced waves; these caused a N_e decrease of 2–3 orders of magnitude at 400-500 km, covered wide longitudinal ranges over 100°, and lasted at least 4–5 hours. These EPBs could be seeded by acoustic-gravity resonance and coupling to less-damped Lamb waves.

Plain Language Summary

The catastrophic 2022 Tonga volcano eruption triggered giant atmospheric waves that propagated into and strongly impacted Earth's ionosphere. Using ground-based multi-GNSS TEC measurements and Swarm satellite observations, we found large-scale, intense ionospheric disturbances. The eruption created a large ionospheric hole near the epicenter embedded with cascading TEC drops and periodic oscillations, resulting from various acoustic-gravity wave impulses. Atmospheric Lamb waves propagated globally at a velocity of ∼315 m/s, coupled to ionosphere heights possibly via acoustic-gravity resonance, and caused global-scale ionospheric disturbances. We report for the first time that strong nighttime equatorial plasma bubbles were observed in the vast Asian-Oceania area over 100° longitudinal range, lasting at least 4–5 hours following the consecutive arrival of volcano-induced waves and the dusk terminator. These results demonstrate far-reaching and long-lasting atmosphere-ionosphere impacts from a devastating natural disaster, and highlight new ways in which surface conditions can impact the upper atmosphere.

1 Introduction

Natural geological disasters such as volcanic eruptions and intense earthquakes can create impulsive forcing near Earth's surface and cause considerable atmospheric pressure waves (e.g., Hines, 1960; Yeh & Liu, 1974; Komjathy et al., 2016). Depending on their velocities and/or frequencies, these atmospheric waves include supersonic shock waves along with acoustic and gravity waves (AGWs). Acoustic waves travel through adiabatic compression and decompression, with frequencies higher than the acoustic cutoff frequency (∼3.3 mHz), periods smaller than 5 min, and radially outward propagating velocity at the sound speed (Astafyeva, 2019; Blanc, 1985). By comparison, gravity waves are triggered by vertical displacement in the ocean surface and atmosphere, with gravity being the predominant restoring force. They are characterized by lower-than-buoyancy frequencies, periods of several to tens of minutes, and obliquely upward propagating pattern with oppositely directed phase and group velocities (Artru et al., 2004; C. Y. Huang et al., 2019). The initial AGWs generated by these events can even reach ionospheric heights with exponentially-increased amplitudes, modulating ionospheric electron density leading to traveling ionospheric disturbances (TIDs) through ion-neutral collisional momentum transfer (e.g., Afraimovich et al., 2010; Chou et al., 2020; Dautermann, Calais, & Mattioli, 2009; Hao et al., 2006; Huba et al., 2015; Inchin et al., 2020; Komjathy et al., 2012; J. Y. Liu et al., 2006; Nishioka et al., 2013; Rolland et al., 2011; Tsugawa et al., 2011; Zettergren et al., 2017).

The rapid development over the past few decades of ground-based Global Navigation Satellite System (GNSS) receiver networks has allowed ionospheric responses to volcano-induced AGWs to be intermittently investigated based on sporadic eruption events. For instance, Roberts et al. (1982) found that ionospheric TIDs after the explosion of Mount St. Helens were detected 4900 km away with various propagation velocities between 350–550 m/s. C. H. Liu et al. (1982) found that some atmospheric perturbations for this same event were capable of travelling globally in the form of Lamb waves. Moreover, Heki (2006) observed that ionospheric total electron content (TEC) disturbances triggered by acoustic waves after the Asamo volcano eruption could propagate as fast as 1.1 km/s. Dautermann, Calais, and Mattioli (2009) and Dautermann, Calais, Lognonné, and Mattioli (2009) found that quasiperiodic TEC oscillations around 4 mHz were detected 18 min after the Soufrière Hill Volcano explosion and lasted 40 min, with various horizontal velocities between 500–700 m/s. Shults et al. (2016) observed that the propagation velocity of ionospheric TEC disturbances after the Calbuco volcano eruption was around 900–1200 m/s, close to acoustic speeds at ionospheric heights. Nakashima et al. (2016) found that harmonic acoustic oscillations created by the Kelud volcano eruption lasted for 2.5 hr with ionosphere disturbances traveling at 800 m/s. These studies in aggregate have greatly informed community knowledge of co-volcanic ionospheric disturbances.

The recent Hunga Tonga-Hunga Ha'apai (herein simplified as Tonga) volcano eruption at 04:14:45 UT on 15 January 2022 was the largest eruption in the last three decades, causing significant wave perturbations from ocean surface to the whole atmosphere across the globe in less than 24 hours (Duncombe, 2022). This event provides a unique scientific opportunity to advance the current understanding of volcano-induced local and global ionospheric responses. So far, prompt studies have provided some initial analyses of ionospheric disturbances after eruption. Themens et al. (2022) analyzed regional and global large-scale and medium-scale TID features following the eruption. Zhang et al. (2022) found global propagation of Lamb waves for three full cycles within four days, and Lin et al. (2022) reported rapid appearance of disturbances in the conjugate Hemisphere.

Despite these important early results, more features of this event remain to be analyzed. In this study, we report a different new phenomenon using both ground-based GNSS TEC and satellite measurements: Pronounced post-volcanic nighttime equatorial plasma bubbles (EPBs) were observed over Asian-Oceania area across 100° longitudes, with magnitude decreased by 2-3 orders and lasted at least 4-5 hours. In particular, this is the first time such dramatic plasma density depletions associated with volcano-induced AGWs has been reported. Our study is also the first to use Beidou Geostationary Orbit (GEO) data for precise TEC measurements at stationary ionosphere pierce points (IPPs) near Tonga and accurate analysis of local ionospheric disturbances. These results are discussed in the following sections.

2 Data and Method Description

GNSS TEC data are produced at Massachusetts Institute of Technology's Haystack Observatory using 5000+ worldwide ground-based receivers, and are provided through the Madrigal distributed data system (Rideout & Coster, 2006; Vierinen et al., 2016). Besides traditional GPS/GLONASS TEC, we also used TEC from 240+ available Beidou receivers, especially from Beidou GEO receivers adjacent to eruption. Beidou GEO TEC data can provide more robust estimation from stationary IPPs in a manner less impacted by complicated ionospheric spatiotemporal variability (Aa et al., 2020).

We used two quantities to investigate ionospheric response to the eruption: (1) Detrended TEC (dTEC), characterizing the wave-like ionospheric oscillations by removing a background variation trend for all satellite-receiver TEC pairs. Detrending is performed using a Savitzky-Golay low-pass filter with a 30-min sliding window (Savitzky & Golay, 1964; Zhang et al., 2017, 2019). (2) Rate of TEC Index (ROTI), describing dynamic ionospheric changes due to plasma irregularities and/or gradients. ROTI is defined as the 5-min standard deviation of the TEC time derivative (Pi et al., 1997; Cherniak et al., 2014; Aa et al., 2019).

Besides ground-based GNSS TEC, we also used in-situ electron density (N_{e}) measurements from the European Space Agency's Swarm constellations (Friis-Christensen et al., 2008; Spicher et al., 2015). Swarm includes three identical satellites that fly in approximately circular orbits at 88° inclination. Swarm A and C fly side-by-side at around 450 km with 1.4° longitudinal separation, and Swarm B fly at around 510 km (Knudsen et al., 2017). Moreover, the infrared brightness cloud temperature data, derived from Geosynchronous Operational Environmental Satellites (GOES) and other selected geostationary satellites (Janowiak et al., 2017), were also used to gauge volcano-related convection activity.

3 Results

3.1 Local Ionospheric Disturbances

Figure 1a shows the volcano epicenter location (20.5°S, 175.4°W) and the great-circle distances from the epicenter at an ionospheric height of 300 km. Also shown are four adjacent Beidou GEO receivers within 1000 km radius: TONG (21.02°S, 175.18°W), LAUT (17.5°S, 177.45°E), SAMO (13.76°S, 171.74°W), and FTNA (14.22°S, 178.12°W). Figure 1b shows a regional view with overlaid infrared brightness cloud temperature at 05 UT on 15 January 2022. The newly-formed dark blue area over Tonga indicates a cold cloud temperature below 220 K, indicating that the initial ash plume protruded into the tropopause in less than 45 mins triggering atmospheric cooling. Also shown are fixed IPPs locations of Beidou GEO satellites C01 and C04 for each receiver.

The unique Beidou GEO observations with stationary IPPs allow us to accurately determine localized temporal ionospheric variations following the eruption (Figures 1c–1f). At TONG, the nearest station to the epicenter, after a minor increase following the eruption, the TEC curves showed three cascading dips as marked by yellow shades. Collectively these formed an integrated depletion hole around 05 UT with amplitude of 5–8 TECU. Smaller periodic oscillations were also embedded in the depletion. Similar to TONG, LAUT TEC curves also exhibited three consecutive dips shortly after the eruption, with a clear phase and time delay between TONG and LAUT as well as between C01 and C04. Since fixed IPP locations from TONG and LAUT (corresponding to C01 and C04) were approximately arrayed radially outward in the same direction away from the epicenter (Figure 1b), we collectively utilized their distance and phase/time information to deduce wave propagation parameters in this localized region. The radial propagation velocity corresponding to these three dips were calculated to be 760 m/s, 470 m/s, and 315 m/s, respectively. For SAMO and FTNA, the radial distances of their GEO IPPs were close, which made detections of oscillation phase and time delay more difficult compared to TONG and LAUT. Nevertheless, significant depletion features occurred through cliff-like TEC drops as large as 10 TECU before local sunset around 0620–0700 UT, and were particularly prominent over SAMO.

To further extract wave-like oscillations embedded in the depletion, Figure 1g plots all detrended Beidou GEO TEC curves in UT-distance coordinates. Volcano-induced fluctuations were generally within 0.5-3 TECU but sometimes reached 6 TECU. The above-mentioned propagation velocities can also be estimated through slanted fiducial lines connecting iso-phase wavefronts at different IPPs. Some smaller-scale oscillations with velocities of 180-250 m/s were registered after major perturbations. By considering TONG measurements alone, another fast travelling wave mode with 1050 m/s speed can be derived by connecting two initial dTEC bumps at C01 and C04, though this wave did not seem to propagate beyond 1000 km. Despite fewer Beidou GEO observations as com-

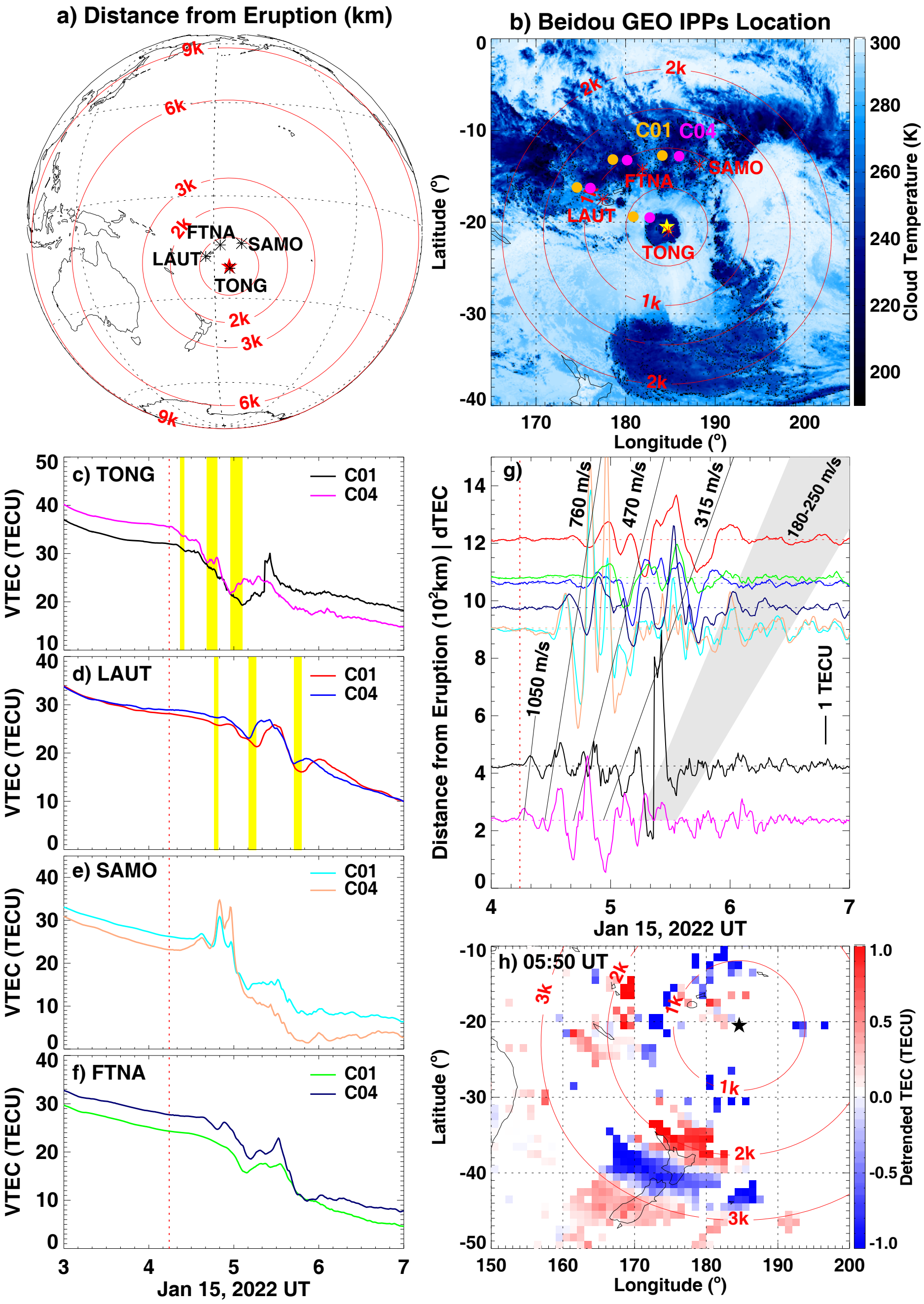

Figure 1. (a) Global view of the Tonga volcano eruption location (star) and four adjacent Beidou GEO receivers (asterisks). The iso-distance circles from the eruption epicenter are shown in red lines. (b) Regional view of above-mentioned information and corresponding Beidou GEO IPPs location for C01 and C04 satellites, overlaid with the deep cloud brightness temperature observations at 05 UT on 15 January 2022. (c–f) Temporal variation of Beidou GEO TEC at four sites. The eruption time is marked by a vertical dotted line. Yellow shades mark three distinct TEC dips using TONG and LAUT measurements as examples. (g) UT-distance variation of detrended Beidou GEO TEC. The vertical line indicates eruption beginning time; the slanted lines and shades indicate different propagation velocities. (h) Observation of concentric TIDs near New Zealand using two-dimensional detrended TEC map.

pared to GPS, these velocity estimations have the key quality of being free from possible spatiotemporal variation contamination associated with normal moving IPPs.

Within the eruption near field, Figure 1h displays a 2-D dTEC map combining multi-GNSS measurements to show concentric TID features over New Zealand at 2000-3000 km distance with an estimated wavelength of 1200-1500 km. These characteristics are generally consistent with recent studies (Themens et al., 2022; Zhang et al., 2022) and will not be described further.

3.2 Global Ionospheric Disturbances

Besides significant local perturbations, ionospheric ripples also propagated globally. Figures 2a–2f show 2-D global ROTI maps at six time steps on 15 January 2022 derived from 5000+ multi-GNSS receivers. At 04:50 UT, large ROTI values manifesting strong ionospheric disturbances were sporadically detected near the epicenter. At 06:35 UT, large disturbances appeared over New Zealand around 3000 km away. At 08:35 UT, signatures of disturbances were found at New Guinea and Hawaiian islands around 5000 km away. At 12:00 UT, traces of ionospheric disturbances were widely registered in the low and midlatitude East Asian sector around 9000 km distance. At 14:00 UT, beside the Asian sector, noticeable disturbance features were simultaneously found both in the North and South American area approximately parallel to the 12,000 km iso-distance line therein. At 16:15 UT, strong disturbance signals further extended into 14,000 km distance in the American sector, and were clearly seen in the Indian sector between 12,000-15,000 km away. Despite data gaps, the outbound propagation of ionospheric disturbances can be clearly seen from these ROTI maps. The full animation of global ROTI variation is attached in the supplementary material.

To compensate for uneven data distribution, Figure 2g uses a time-distance ROTI plot to identify and trace disturbance propagation, utilizing all available measurements. Note that high-latitude ROTI data above 65° geomagnetic latitude were excluded to eliminate space weather impacts as much as possible. Two significant features can be observed: (1) Volcano-induced ionospheric disturbances travelled globally to at least 16,000 km away from the epicenter. Through calculating the slope of the fitted line along the discernible boundary, the global propagation velocity of ionospheric ROTI disturbances is about 315 ± 15 m/s. This is consistent with one of the major disturbance velocities (i.e., 315 m/s) derived using Beidou GEO TEC. (2) Moderate-to-high ROTI values (>0.25), consistent with strong ionospheric irregularities and/or gradients, predominantly occurred between 5000–10000 km range around 10–17 UT, following the arrival of volcano-induced wavefronts. These data were mainly contributed by Asian-Oceania area as shown in 2-D ROTI maps. We next further analyze these propagation and irregularity features.

For propagation features, Figures 3a–3i display nine consecutive ROTI maps over the American sector between 13:35–16:15 UT. The wave propagation signatures can be clearly seen via structure movement in higher-than-background ROTI values. The wavefronts were aligned parallel to iso-distance lines with two distinct ends over data-dense regions, especially the one over continental US. The wavefronts propagated outbound from $\sim$11,000 km to $\sim$14,000 km with an average velocity of 315 m/s, consistent with the time-distance plot (Figure 2g) and Beidou TEC results (Figure 1g).

For irregularity features, Figures 3j–3r show nine ROTI maps over the Asian sector. Ionospheric irregularities were quite noticeable around the equatorial ionization anomaly (EIA) crests, which extended westbound from Indonesia, Philippines, and the Japan archipelago around 11:00 UT all the way to India and Bay of Bengal around 15–16 UT. Utilizing spaceborne observations, Figures 4a and 4c show ten consecutive paths of Swarm B and Swarm C satellite that flew in the premidnight local time sector over Asian-Oceania area, overlaying on top of background ROTI maps. Figures 4b and 4d display the corresponding geomagnetic latitudinal profiles of in-situ N_{e} along these paths between 11–18 UT, with

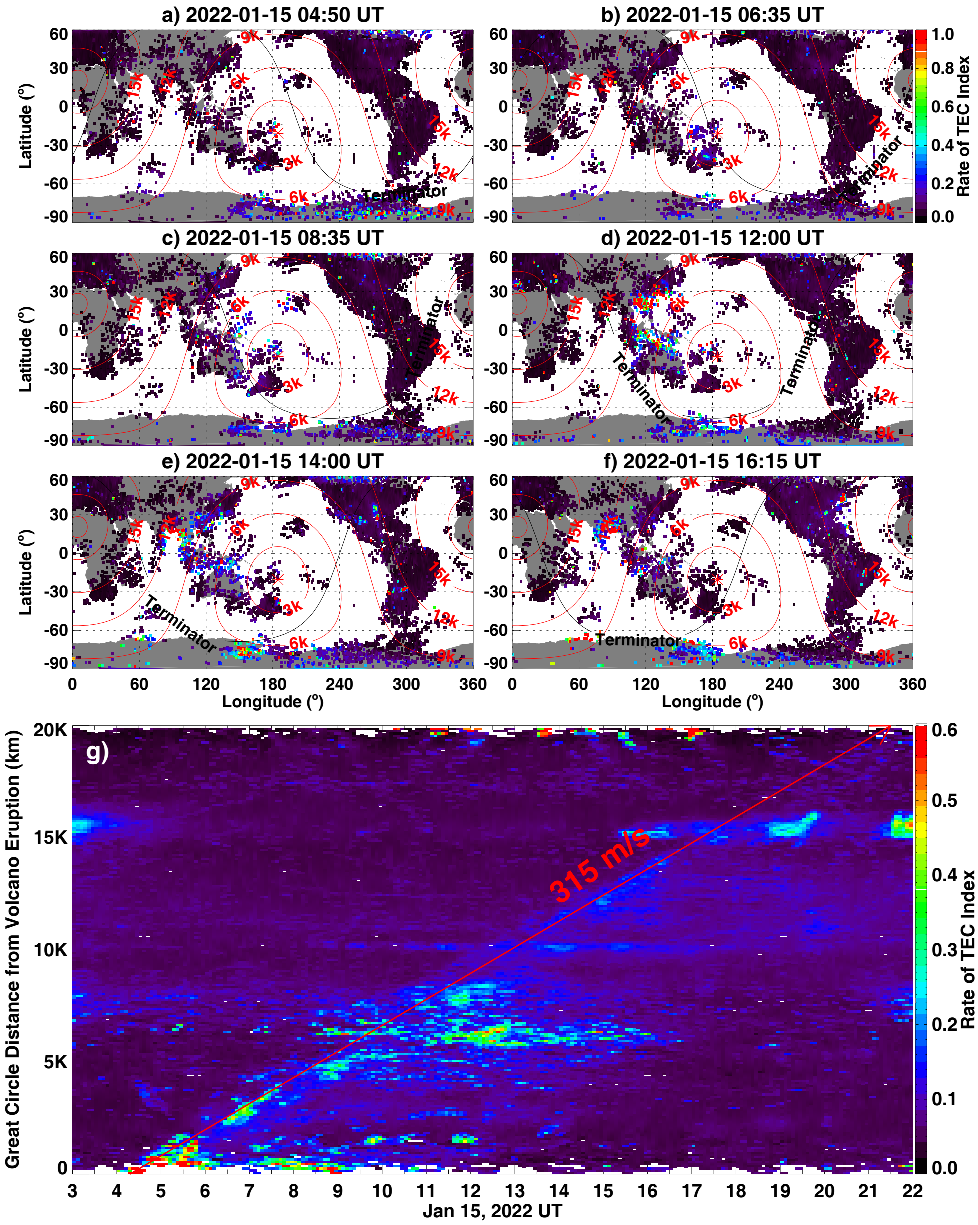

Figure 2. (a–f) Global 2-D ROTI maps at six time steps on January 15, 2022. The volcano eruption location (asterisk), iso-distance lines from eruption (red lines), and solar terminator (black line) are marked, respectively. (g) UT-distance variation of ROTI values.

reference background N_e profiles from the previous day also plotted. In concert with high ROTI values, significant equatorial and low-latitude plasma bite-outs with density as low as 10^2–10^3 cm^{-3} were quite obvious in these profiles, which were 2–3 orders of magnitude lower than reference levels. These data indicate that strong EPBs formed at local postsunset. This is reported for the first time after an extreme volcano eruption, and will be further discussed in the next section.

4 Discussion

Beidou GEO TEC observing geometries provided a unique opportunity to continuously observe and precisely evaluate the volcano-induced local ionosphere characteristics using fixed IPPs. The most direct feature near the epicenter were significant TEC depletion of 5–10 TECU formed by consecutive cliff-like drops with duration of ∼1 hr. A similar phenomenon of a transient co-seismic ionospheric "hole" near the epicenter has been occasionally reported before (e.g., Kakinami et al., 2012; Saito et al., 2011; Tsugawa et al., 2011), but its mechanism is still under debate. Kakinami et al. (2012) suggested that this is a tsunami-related depletion induced by ionosphere descent and recombination enhancement through meter-scale sea surface downwelling at the tsunami source region. However, Kamogawa et al. (2015) indicated this depletion could instead occur after a large inland earthquake. Moreover, numerical simulation results given by Shinagawa et al. (2013) and Zettergren et al. (2017) collectively indicated that the TEC depletion was more likely to be caused by strong expansion and upwelling in the thermosphere along with outward ionospheric plasma flow driven by impulsive nonlinear acoustic wave pulses. This latter mechanism helps explain our direct observational evidence in this Tonga event: the local TEC depletion was composed of cascading decreases that correspond to different acoustic wave impulses.

Besides the large depletion, several acoustic-gravity oscillation modes with different propagation velocities were identified. The fast modes with 1050 m/s and 760 m/s, arising from different excitation conditions, fall within the sound speed range at ionospheric heights and are comparable to prior studies (e.g., Calais et al., 1998; Heki & Ping, 2005; Heki, 2006; Otsuka et al., 2006). These modes are considered to be caused by acoustic pressure waves generated from the sea surface at the epicenter (Astafyeva, 2019; Chen et al., 2011; Tsugawa et al., 2011). The subsequent medium-speed modes between 300-500 m/s range could be associated with lower-frequency infrasonic and/or gravity parts of AGWs, which propagated to at least 3500 km away as deduced from Figure 1h. The ionospheric disturbances also included a slower propagation mode with speeds of 180-250 m/s, due to gravity waves triggered by tsunami–atmosphere–ionosphere coupling processes (e.g., Artru et al., 2005; Azeem et al., 2017; Huba et al., 2015; Savastano et al., 2017; Meng et al., 2018).

Volcano-induced acoustic-gravity resonance and ionospheric disturbances exhibited significant and far-reaching impacts. The 315 m/s mode showed the most distinct global-scale travelling signature, reaching 16,000+ km away from the epicenter. C. H. Liu et al. (1982) reported that the volcano explosion of Mount St. Helen caused worldwide surface pressure oscillations and ionospheric perturbations at far as 10,000 km away from the epicenter, which can only be explained in terms of Lamb waves with a horizontal propagation velocity between 300-310 m/s. The occurrence of atmospheric Lamb waves was also reported after the gigantic Kratatoa volcanic eruption in 1883 (Symons, 1888; Pekeris, 1939). Lamb waves in the millihertz frequency band could be excited by surface air pressure perturbation due to significant geological/meteorological events, and could propagate long distances with little attenuation at a sound speed of ∼310 m/s (Bretherton, 1969; Lindzen & Blake, 1972). Despite the fact that Lamb waves are normally concentrated within a few scale heights in the troposphere/stratosphere, their energy can tunnel into the thermosphere via acoustic-gravity resonance at certain frequencies and thus may further cause ionospheric disturbances (Nishida et al., 2014). Our Beidou GEO TEC

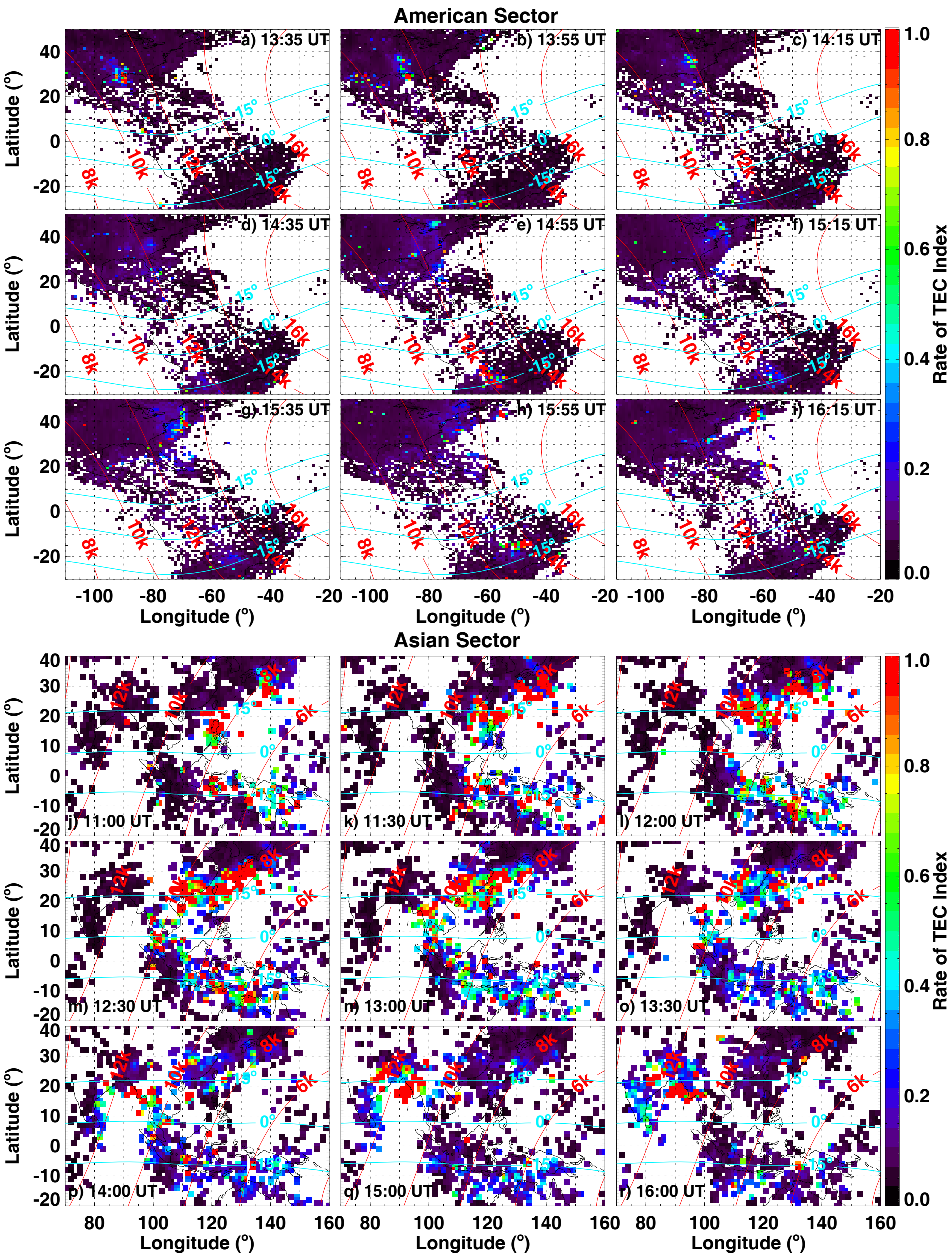

Figure 3. 2-D ROTI maps over (a–i) American and (j–r) Asian sectors at nine different time steps on January 15, 2022. The iso-distance lines (red) and geomagnetic equator and ±15° lines (cyan) are also marked.

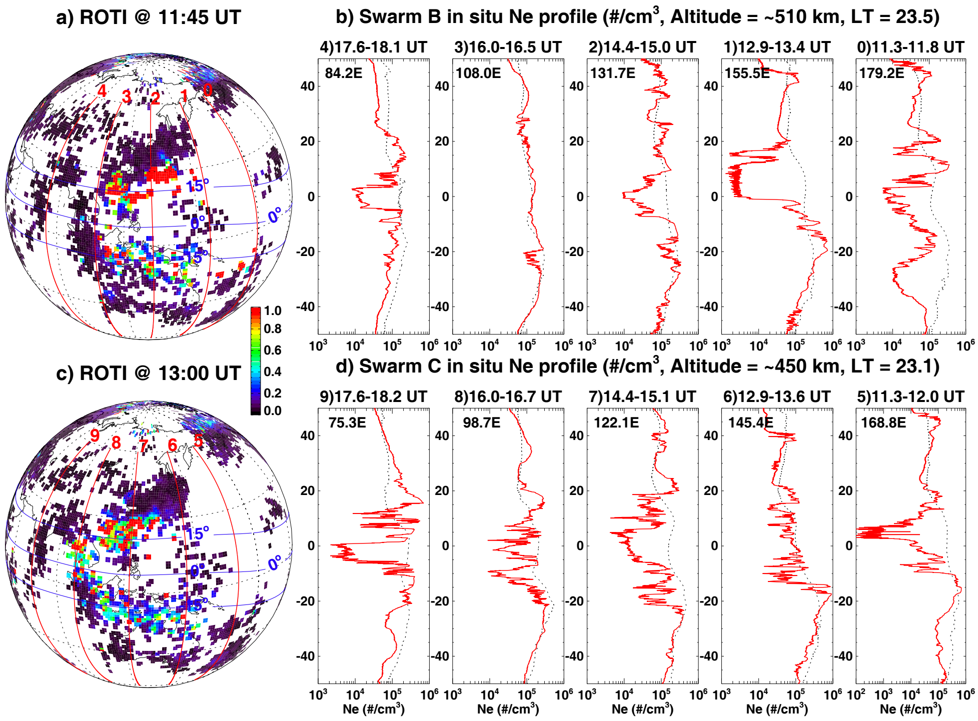

Figure 4. (a) The global ROTI map focusing on Asian sector at 11:45 UT on 15 January 2022 with five consecutive Swarm B paths. The magnetic equator and $\pm 15^o$ lines are marked by blue lines. (b) Variation of in situ electron density as a function of geomagnetic latitudes along these paths (red lines). The black dotted lines show the corresponding reference profiles from the previous day. (c, d) The same as Figures 4a and 4b, respectively, but for ROTI map at 13:00 UT and Swarm C paths.

observations and global multi-GNSS ROTI results collectively demonstrate the robust and long-distance propagation of ionospheric shock fronts with a velocity of $\sim$315 m/s. They also provide new evidence verifying the existence and globally propagating nature of atmospheric Lamb waves following recent initial corroborations (Zhang et al., 2022; Themens et al., 2022; Lin et al., 2022).

The last and most significant discovery of this study is the presence of strong and long-lasting post-volcanic EPBs over the Asian-Oceania area, spanning a wide longitudinal range over 100° with duration $\geq$4–5 hours and N_e decrease of 2–3 orders of magnitude at 400–500 km. EPBs are large-scale plasma density depletions that usually form in the postsunset bottomside F region at the equatorial and low-latitude ionosphere, under favorable conditions of prereversal enhancement (PRE) and increased Rayleigh-Taylor instability with steep vertical density gradients after the decay of E region (e.g., Abdu, 2005; Aa et al., 2019; Karan et al., 2020). One of the most important seeding factors of EPBs is atmospheric gravity waves, which form large-scale wave structures in the bottomside F region and provide initial modulations in the electron density and/or polarization electric field perturbations for EPBs development (e.g., C.-S. Huang & Kelley, 1996; Krall et al., 2013; Huba & Liu, 2020; Tsunoda, 2010). Although co-seismic and co-volcanic AGWs and associated ionospheric oscillations have been widely reported, to the best of our knowledge, such widespread and long-lasting post-volcanic EPB features have never been reported before. Moreover, despite a minor geomagnetic storm at the end of January 14 with Kp index reaching 5+, the interplanetary magnetic field Bz was close to zero between 04-14 UT on January 15, with no hints of a large penetration electric field prior to observed dusktime EPBs. The possibility of strong magnetospheric driving forces for EPBs was thus unlikely in this situation. The volcano eruption occurred at 17:14 Local time (04:14 UT), and the AGW resonance and coupling with Lamb waves propagated at 315±15 m/s. Thus, westbound wavefronts and the dusk terminator swept over the wide Asian-Oceania area almost consecutively, which maximized the EPBs seeding under favorable PRE. Besides the direct seeding role, the gravity wave amplitude is known to increase exponentially with altitude due to decreasing atmospheric density, thus large-scale gravity resonance could modulate F layer heights to elevate and destabilize bottomside density gradients (Abdu et al., 2009). In aggregate, these factors effectively catalyzed and amplified initial density perturbation, leading to pronounced long-lasting EPBs in the equatorial and low-latitude Asian-Oceania area.

5 Conclusions

Local and global ionospheric disturbances associated with the 2022 Tonga volcano eruption were studied using both ground-based and space-borne observations, including Beidou GEO TEC from fixed IPPs, multi-GNSS ROTI data, and Swarm in-situ N_e measurements. The main results and findings are as follows:

1. The volcano eruption resulted in significant local ionospheric depletion of 5–10 TECU near the epicenter that consisted of cascading TEC decreases and oscillations. This was likely caused by strong thermosphere expansion and large ionosphere outward flow via neutral drag driven by co-volcanic consecutive shock-acoustic wave pulses.

2. We observed both local and distant ionospheric large-amplitude disturbances due to various volcano-induced AGW modes with different phase velocities, including fast acoustic modes of 1050 m/s and 760 m/s, infrasonic mode of 460 m/s, atmospheric Lamb waves mode of 315 m/s, and tsunami-gravity modes of 180–250 m/s. The atmospheric Lamb waves mode exhibited the most distinct long-distance travelling feature reaching at least 16,000 km away from the epicenter, causing significant global-scale ionospheric disturbances via acoustic-gravity resonance and wave coupling.

3. For the first time, we observed pronounced and prolonged post-volcanic nighttime EPBs over the Asian-Oceania area following the arrival of Lamb waves, with N_e decreased by 2–3 orders of magnitude at 400-500 km. EPBs covered wide longitudinal areas over 100° and lasted at least 4–5 hours. Given that the westbound wavefront and dusk terminator swept over the Asian-Oceania area consecutively, significant EPBs were likely seeded by gravity resonance and coupling with less-damped Lamb waves, under the right timing with favorable conditions of postsunset PRE and the Rayleigh-Taylor instability.

Data Availability Statement

GNSS TEC data products are provided through the Madrigal distributed data system at (`http://cedar.openmadrigal.org/`) by MIT. Multi-GNSS experiment data are provided by NASA Crustal Dynamics Data Information System (CDDIS) (`https://cddis.nasa.gov/`). Swarm data are provide by European Space Agency (`https://swarm-diss.eo.esa.int/`). The cloud brightness temperature data are provided by NASA Goddard Earth Sciences Data and Information Services Central (`https://disc.gsfc.nasa.gov/`).

Acknowledgments

GNSS TEC data are part of the U.S. NSF's Millstone Hill Geospace Facility program under AGS-1952737 with MIT. We acknowledge NSF awards AGS-2033787 and PHY-2028125, NASA support 80NSSC22K0171, 80NSSC21K1310, 80NSSC21K1775, and 80NSSC19K0834, AFOSR MURI Project FA9559-16-1-0364, and ONR Grant N00014-17-1-2186. Data for TEC processing is provided from the following organizations: UNAVCO, SOPAC, IGN (France), IGS, CDDIS, NGS, IBGE (Brazil), RAMSAC (Argentina), CORS (Panama), Arecibo Observatory, LISN, Topcon, CHAIN (Canada), CRS (Italy), SONEL, RENAG (New Zealand), GNSS Reference Networks, Finnish Meteorological Institute, and SWEPOS.

References

Aa, E., Zhang, S.-R., Erickson, P. J., Goncharenko, L. P., Coster, A. J., Jonah, O. F., . . . Liu, L. (2020, November). Coordinated Ground-Based and Space-Borne Observations of Ionospheric Response to the Annular Solar Eclipse on 26 December 2019. *Journal of Geophysical Research: Space Physics*, *125*(11), e28296. doi: 10.1029/2020JA028296

Aa, E., Zou, S., Ridley, A., Zhang, S., Coster, A. J., Erickson, P. J., . . . Ren, J. (2019, February). Merging of Storm Time Midlatitude Traveling Ionospheric Disturbances and Equatorial Plasma Bubbles. *Space Weather*, *17*(2), 285-298. doi: 10.1029/2018SW002101

Abdu, M. A. (2005). Equatorial ionosphere thermosphere system: Electrodynamics and irregularities. *Adv. Space Res.*, *35*, 771-787. doi: 10.1016/j.asr.2005.03.150

Abdu, M. A., Alam Kherani, E., Batista, I. S., de Paula, E. R., Fritts, D. C., & Sobral, J. H. A. (2009, July). Gravity wave initiation of equatorial spread F/plasma bubble irregularities based on observational data from the SpreadFEx campaign. *Annales Geophysicae*, *27*(7), 2607-2622. doi: 10.5194/angeo-27-2607-2009

Afraimovich, E. L., Feng, D., Kiryushkin, V. V., & Astafyeva, E. I. (2010, November). Near-field TEC response to the main shock of the 2008 Wenchuan earthquake. *Earth, Planets and Space*, *62*(11), 899-904. doi: 10.5047/eps.2009.07.002

Artru, J., Ducic, V., Kanamori, H., Lognonné, P., & Murakami, M. (2005, March).

Ionospheric detection of gravity waves induced by tsunamis. *Geophysical Journal International*, *160*(3), 840-848. doi: 10.1111/j.1365-246X.2005.02552.x

Artru, J., Farges, T., & Lognonné, P. (2004, September). Acoustic waves generated from seismic surface waves: propagation properties determined from Doppler sounding observations and normal-mode modelling. *Geophysical Journal International*, *158*(3), 1067-1077. doi: 10.1111/j.1365-246X.2004.02377.x

Astafyeva, E. (2019, December). Ionospheric Detection of Natural Hazards. *Reviews of Geophysics*, *57*(4), 1265-1288. doi: 10.1029/2019RG000668

Azeem, I., Vadas, S. L., Crowley, G., & Makela, J. J. (2017, March). Traveling ionospheric disturbances over the United States induced by gravity waves from the 2011 Tohoku tsunami and comparison with gravity wave dissipative theory. *Journal of Geophysical Research: Space Physics*, *122*(3), 3430-3447. doi: 10.1002/2016JA023659

Blanc, E. (1985, December). Observations in the upper atmosphere of infrasonic waves from natural or artificial sources - A summary. *Annales Geophysicae*, *3*, 673-687.

Bretherton, F. P. (1969, October). Lamb waves in a nearly isothermal atmosphere. *Quarterly Journal of the Royal Meteorological Society*, *95*(406), 754-757. doi: 10.1002/qj.49709540608

Calais, E., Bernard Minster, J., Hofton, M., & Hedlin, M. (1998, January). Ionospheric signature of surface mine blasts from Global Positioning System measurements. *Geophysical Journal International*, *132*(1), 191-202. doi: 10.1046/j.1365-246X.1998.00438.x

Chen, C. H., Saito, A., Lin, C. H., Liu, J. Y., Tsai, H. F., Tsugawa, T., … Matsumura, M. (2011, July). Long-distance propagation of ionospheric disturbance generated by the 2011 off the Pacific coast of Tohoku Earthquake. *Earth, Planets and Space*, *63*(7), 881-884. doi: 10.5047/eps.2011.06.026

Cherniak, I., Krankowski, A., & Zakharenkova, I. (2014, August). Observation of the ionospheric irregularities over the Northern Hemisphere: Methodology and service. *Radio Sci.*, *49*, 653-662. doi: 10.1002/2014RS005433

Chou, M.-Y., Cherniak, I., Lin, C. C. H., & Pedatella, N. M. (2020, April). The Persistent Ionospheric Responses Over Japan After the Impact of the 2011 Tohoku Earthquake. *Space Weather*, *18*(4), e02302. doi: 10.1029/2019SW002302

Dautermann, T., Calais, E., Lognonné, P., & Mattioli, G. S. (2009, December). Lithosphere-atmosphere-ionosphere coupling after the 2003 explosive eruption of the Soufriere Hills Volcano, Montserrat. *Geophysical Journal International*, *179*(3), 1537-1546. doi: 10.1111/j.1365-246X.2009.04390.x

Dautermann, T., Calais, E., & Mattioli, G. S. (2009, February). Global Positioning System detection and energy estimation of the ionospheric wave caused by the 13 July 2003 explosion of the Soufrière Hills Volcano, Montserrat. *Journal of Geophysical Research: Solid Earth*, *114*(B2), B02202. doi: 10.1029/2008JB005722

Duncombe, J. (2022). The surprising reach of Tonga's giant atmospheric waves. *Eos: AGU Science News*, *103*. Retrieved from `https://doi.org/10.1029/2022EO220050`

Friis-Christensen, E., Lühr, H., Knudsen, D., & Haagmans, R. (2008, January). Swarm-An Earth Observation Mission investigating Geospace. *Advances in Space Research*, *41*(1), 210-216. doi: 10.1016/j.asr.2006.10.008

Hao, Y.-Q., Xiao, Z., & Zhang, D.-H. (2006, July). Responses of the Ionosphere to the Great Sumatra Earthquake and Volcanic Eruption of Pinatubo. *Chinese Physics Letters*, *23*(7), 1955-1957. doi: 10.1088/0256-307X/23/7/082

Heki, K. (2006, July). Explosion energy of the 2004 eruption of the Asama Volcano, central Japan, inferred from ionospheric disturbances. *Geophysical Research Letters*, *33*(14), L14303. doi: 10.1029/2006GL026249

Heki, K., & Ping, J. (2005, August). Directivity and apparent velocity of the coseismic ionospheric disturbances observed with a dense GPS array. *Earth and Planetary Science Letters*, *236*(3-4), 845-855. doi: 10.1016/j.epsl.2005.06.010

Hines, C. O. (1960, January). Internal atmospheric gravity waves at ionospheric heights. *Canadian Journal of Physics*, *38*, 1441. doi: 10.1139/p60-150

Huang, C.-S., & Kelley, M. C. (1996, January). Nonlinear evolution of equatorial spread F. 1. On the role of plasma instabilities and spatial resonance associated with gravity wave seeding. *Journal of Geophysical Research*, *101*(A1), 283-292. doi: 10.1029/95JA02211

Huang, C. Y., Helmboldt, J. F., Park, J., Pedersen, T. R., & Willemann, R. (2019, March). Ionospheric Detection of Explosive Events. *Reviews of Geophysics*, *57*(1), 78-105. doi: 10.1029/2017RG000594

Huba, J. D., Drob, D. P., Wu, T. W., & Makela, J. J. (2015, July). Modeling the ionospheric impact of tsunami-driven gravity waves with SAMI3: Conjugate effects. *Geophysical Research Letters*, *42*(14), 5719-5726. doi: 10.1002/2015GL064871

Huba, J. D., & Liu, H. L. (2020, July). Global Modeling of Equatorial Spread F with SAMI3/WACCM-X. *Geophysical Research Letters*, *47*(14), e88258. doi: 10.1029/2020GL088258

Inchin, P. Â. A., Snively, J. Â. B., Zettergren, M. Â. D., Komjathy, A., Verkhoglyadova, O. Â. P., & Tulasi Ram, S. (2020, April). Modeling of Ionospheric Responses to Atmospheric Acoustic and Gravity Waves Driven by the 2015 Nepal Mw7.8 Gorkha Earthquake. *Journal of Geophysical Research: Space Physics*, *125*(4), e27200. doi: 10.1029/2019JA027200

Janowiak, J., Joyce, B., & Xie, P. (2017). *Ncep/cpc l3 half hourly 4km global (60s - 60n) merged ir v1.* NASA Goddard Earth Sciences Data and Information Services Center. doi: 10.5067/P4HZB9N27EKU

Kakinami, Y., Kamogawa, M., Tanioka, Y., Watanabe, S., Riadi Gusman, A., Liu, J.-Y., … Mogi, T. (2012, January). Tsunamigenic ionospheric hole. *Geophysical Research Letters*, *39*, L00G27. doi: 10.1029/2011GL050159

Kamogawa, M., Kanaya, T., Orihara, Y., Toyoda, A., Suzuki, Y., Togo, S., & Liu, J.-Y. (2015, November). Does an ionospheric hole appear after an inland earthquake? *Journal of Geophysical Research: Space Physics*, *120*(11), 9998-10. doi: 10.1002/2015JA021476

Karan, D. K., Daniell, R. E., England, S. L., Martinis, C. R., Eastes, R. W., Burns, A. G., & McClintock, W. E. (2020, September). First Zonal Drift Velocity Measurement of Equatorial Plasma Bubbles (EPBs) From a Geostationary Orbit Using GOLD Data. *Journal of Geophysical Research: Space Physics*, *125*(9), e28173. doi: 10.1029/2020JA028173

Knudsen, D. J., Burchill, J. K., Buchert, S. C., Eriksson, A. I., Gill, R., Wahlund, J. E., … Moffat, B. (2017, February). Thermal ion imagers and Langmuir probes in the Swarm electric field instruments. *Journal of Geophysical Research: Space Physics*, *122*(2), 2655-2673. doi: 10.1002/2016JA022571

Komjathy, A., Galvan, D. A., Stephens, P., Butala, M. D., Akopian, V., Wilson, B., … Hickey, M. (2012, December). Detecting ionospheric TEC perturbations caused by natural hazards using a global network of GPS receivers: The Tohoku case study. *Earth, Planets and Space*, *64*(12), 1287-1294. doi: 10.5047/eps.2012.08.003

Komjathy, A., Yang, Y.-M., Meng, X., Verkhoglyadova, O., Mannucci, A. J., & Langley, R. B. (2016). Review and perspectives: Understanding natural-hazards-generated ionospheric perturbations using gps measurements and coupled modeling. *Radio Science*, *51*(7), 951-961. doi: https://doi.org/10.1002/2015RS005910

Krall, J., Huba, J. D., & Fritts, D. C. (2013, February). On the seeding of equatorial spread F by gravity waves. *Geophysical Research Letters*, *40*(4), 661-664. doi:

10.1002/grl.50144
Lin, J.-T., Rajesh, P. K., Lin, C. C. H., Chou, M.-Y., Liu, J.-Y., Yue, J., ... Kung, M.-M. (2022). Rapid Conjugate Appearance of the Giant Ionospheric Lamb Wave in the Northern Hemisphere After Hunga-Tonga Volcano Eruptions. *Earth and Space Science Open Archive*, 18. Retrieved from `https://doi.org/10.1002/essoar.10510440.2` doi: 10.1002/essoar.10510440.2

Lindzen, R. S., & Blake, D. (1972, January). Lamb waves in the presence of realistic distributions of temperature and dissipation. *Journal of Geophysical Research*, *77*(12), 2166. doi: 10.1029/JC077i012p02166

Liu, C. H., Klostermeyer, J., Yeh, K. C., Jones, T. B., Robinson, T., Holt, O., ... Kersley, L. (1982, August). Global dynamic responses of the atmosphere to the eruption of Mount St. Helens on May 18, 1980. *Journal of Geophysical Research*, *87*(A8), 6281-6290. doi: 10.1029/JA087iA08p06281

Liu, J. Y., Tsai, Y. B., Chen, S. W., Lee, C. P., Chen, Y. C., Yen, H. Y., ... Liu, C. (2006, January). Giant ionospheric disturbances excited by the M9.3 Sumatra earthquake of 26 December 2004. *Geophysical Research Letters*, *33*(2), L02103. doi: 10.1029/2005GL023963

Meng, X., Verkhoglyadova, O. P., Komjathy, A., Savastano, G., & Mannucci, A. J. (2018, September). Physics-Based Modeling of Earthquake-Induced Ionospheric Disturbances. *Journal of Geophysical Research: Space Physics*, *123*(9), 8021-8038. doi: 10.1029/2018JA025253

Nakashima, Y., Heki, K., Takeo, A., Cahyadi, M. N., Aditiya, A., & Yoshizawa, K. (2016, January). Atmospheric resonant oscillations by the 2014 eruption of the Kelud volcano, Indonesia, observed with the ionospheric total electron contents and seismic signals. *Earth and Planetary Science Letters*, *434*, 112-116. doi: 10.1016/j.epsl.2015.11.029

Nishida, K., Kobayashi, N., & Fukao, Y. (2014, January). Background Lamb waves in the Earth's atmosphere. *Geophysical Journal International*, *196*(1), 312-316. doi: 10.1093/gji/ggt413

Nishioka, M., Tsugawa, T., Kubota, M., & Ishii, M. (2013, November). Concentric waves and short-period oscillations observed in the ionosphere after the 2013 Moore EF5 tornado. *Geophysical Research Letters*, *40*(21), 5581-5586. doi: 10.1002/2013GL057963

Otsuka, Y., Kotake, N., Tsugawa, T., Shiokawa, K., Ogawa, T., Effendy, ... Komolmis, T. (2006, February). GPS detection of total electron content variations over Indonesia and Thailand following the 26 December 2004 earthquake. *Earth, Planets and Space*, *58*, 159-165. doi: 10.1186/BF03353373

Pekeris, C. L. (1939, July). The Propagation of a Pulse in the Atmosphere. *Proceedings of the Royal Society of London Series A*, *171*(947), 434-449. doi: 10.1098/rspa.1939.0076

Pi, X., Mannucci, A. J., Lindqwister, U. J., & Ho, C. M. (1997, September). Monitoring of global ionospheric irregularities using the Worldwide GPS Network. *Geophysical Research Letters*, *24*(18), 2283-2286. doi: 10.1029/97GL02273

Rideout, W., & Coster, A. (2006). Automated gps processing for global total electron content data. *GPS Solut.*, *10*(3), 219-228. doi: 10.1007/s10291-006-0029-5

Roberts, D. H., Klobuchar, J. A., Fougere, P. F., & Hendrickson, D. H. (1982, August). A large-amplitude traveling ionospheric distrubance produced by the May 18, 1980, explosion of Mount St. Helens. *Journal of Geophysical Research*, *87*(A8), 6291-6301. doi: 10.1029/JA087iA08p06291

Rolland, L. M., Lognonné, P., Astafyeva, E., Kherani, E. A., Kobayashi, N., Mann, M., & Munekane, H. (2011, July). The resonant response of the ionosphere imaged after the 2011 off the Pacific coast of Tohoku Earthquake. *Earth, Planets and Space*, *63*(7), 853-857. doi: 10.5047/eps.2011.06.020

Saito, A., Tsugawa, T., Otsuka, Y., Nishioka, M., Iyemori, T., Matsumura, M., ...

Choosakul, N. (2011, July). Acoustic resonance and plasma depletion detected by GPS total electron content observation after the 2011 off the Pacific coast of Tohoku Earthquake. *Earth, Planets and Space*, *63*(7), 863-867. doi: 10.5047/eps.2011.06.034

Savastano, G., Komjathy, A., Verkhoglyadova, O., Mazzoni, A., Crespi, M., Wei, Y., & Mannucci, A. J. (2017, April). Real-Time Detection of Tsunami Ionospheric Disturbances with a Stand-Alone GNSS Receiver: A Preliminary Feasibility Demonstration. *Scientific Reports*, *7*, 46607. doi: 10.1038/srep46607

Savitzky, A., & Golay, M. J. E. (1964, January). Smoothing and differentiation of data by simplified least squares procedures. *Analytical Chemistry*, *36*, 1627-1639.

Shinagawa, H., Tsugawa, T., Matsumura, M., Iyemori, T., Saito, A., Maruyama, T., ... Otsuka, Y. (2013, October). Two-dimensional simulation of ionospheric variations in the vicinity of the epicenter of the Tohoku-oki earthquake on 11 March 2011. *Geophysical Research Letters*, *40*(19), 5009-5013. doi: 10.1002/2013GL057627

Shults, K., Astafyeva, E., & Adourian, S. (2016, October). Ionospheric detection and localization of volcano eruptions on the example of the April 2015 Calbuco events. *Journal of Geophysical Research: Space Physics*, *121*(10), 10,303-10,315. doi: 10.1002/2016JA023382

Spicher, A., Cameron, T., Grono, E. M., Yakymenko, K. N., Buchert, S. C., Clausen, L. B. N., ... Moen, J. I. (2015, January). Observation of polar cap patches and calculation of gradient drift instability growth times: A Swarm case study. *Geophysical Research Letters*, *42*(2), 201-206. doi: 10.1002/2014GL062590

Symons, G. J. (1888). The Eruption of Krakatoa and Subsequent Phenomena. *Quarterly Journal of the Royal Meteorological Society*, *14*(68), 301-307. doi: https://doi.org/10.1002/qj.4970146809

Themens, D. R., Watson, C., Žagar, N., Vasylkevych, S., Elvidge, S., Mccaffrey, A., ... Jayachandran, P. T. (2022). Global propagation of ionospheric disturbances associated with the 2022 Tonga Volcanic Eruption. *Earth and Space Science Open Archive*, 25. Retrieved from `https://doi.org/10.1002/essoar.10510350.1` doi: 10.1002/essoar.10510350.1

Tsugawa, T., Saito, A., Otsuka, Y., Nishioka, M., Maruyama, T., Kato, H., ... Murata, K. T. (2011, July). Ionospheric disturbances detected by GPS total electron content observation after the 2011 off the Pacific coast of Tohoku Earthquake. *Earth, Planets and Space*, *63*(7), 875-879. doi: 10.5047/eps.2011.06.035

Tsunoda, R. T. (2010, May). On seeding equatorial spread F: Circular gravity waves. *Geophysical Research Letters*, *37*(10), L10104. doi: 10.1029/2010GL043422

Vierinen, J., Coster, A. J., Rideout, W. C., Erickson, P. J., & Norberg, J. (2016). Statistical framework for estimating GNSS bias. *Atmospheric Measurement Techniques*, *9*, 1303-1312. doi: 10.5194/amt-9-1303-2016

Yeh, K. C., & Liu, C. H. (1974, May). Acoustic-Gravity Waves in the Upper Atmosphere. *Reviews of Geophysics and Space Physics*, *12*, 193. doi: 10.1029/RG012i002p00193

Zettergren, M. D., Snively, J. B., Komjathy, A., & Verkhoglyadova, O. P. (2017, February). Nonlinear ionospheric responses to large-amplitude infrasonic-acoustic waves generated by undersea earthquakes. *Journal of Geophysical Research: Space Physics*, *122*(2), 2272-2291. doi: 10.1002/2016JA023159

Zhang, S.-R., Erickson, P. J., Coster, A. J., Rideout, W., Vierinen, J., Jonah, O., & Goncharenko, L. P. (2019, December). Subauroral and Polar Traveling Ionospheric Disturbances During the 7-9 September 2017 Storms. *Space Weather*, *17*(12), 1748-1764. doi: 10.1029/2019SW002325

Zhang, S.-R., Erickson, P. J., Goncharenko, L. P., Coster, A. J., Rideout, W., &

Vierinen, J. (2017, December). Ionospheric Bow Waves and Perturbations Induced by the 21 August 2017 Solar Eclipse. *Geophysical Research Letters*, *44*(24), 12,067-12,073. doi: 10.1002/2017GL076054

Zhang, S.-R., Vierinen, J., Aa, E., Goncharenko, L. P., Erickson, P. J., Rideout, W., ... Spicher, A. (2022). 2022 Tonga volcanic eruption induced global propagation of ionospheric disturbances via Lamb waves. *Earth and Space Science Open Archive*, 15. Retrieved from `https://doi/abs/10.1002/essoar.10510445.1` doi: 10.1002/essoar.10510445.1